Nontrivial Raman characteristics in 2D non van-der-Waals Mo_5N_6

Ching-Hsiang Yao,† Hongze Gao,† Lu Ping,† Desman Perdamaian Gulo,‡
Hsiang-Lin Liu,‡ Nguyen Tuan Hung,¶ Riichiro Saito,∗,§,‡ and Xi Ling∗,†,‖,⊥

†*Department of Chemistry, Boston University, Boston, Massachusetts 02215, United States*
‡*Department of Physics, National Taiwan Normal University, Taipei 11677, Taiwan*
¶*Frontier Research Institute for Interdisciplinary Sciences, Tohoku University, Sendai 980-8578, Japan*
§*Department of Physics, Tohoku University, Sendai 980-8578, Japan*
‖*Division of Materials Science and Engineering, Boston University, Boston, Massachusetts 02215, United States*
⊥*Photonics Center, Boston University, Boston, Massachusetts 02215, United States*

E-mail: r.saito.sendai@gmail.com; xiling@bu.edu

Abstract

We report resonant Raman spectra of two-dimensional (2D) molybdenum nitrides (Mo_5N_6) with thicknesses ranging from a few to tens of nanometers. 15 Raman peaks are observed experimentally, which further assigned with the density functional theory (DFT) calculation and angular-dependent Raman on the most stable structure of Mo_5N_6 (i.e. AABB-stacking), except for the most intense peak (215 cm^{-1}). We further perform the in-depth investigation of the 215 cm^{-1} through both laser energy and thickness dependent Raman spectrosocpy measurements. No laser energy dependent is observed for 266 nm, 532 nm, and 785 nm laser excitations, excluding the origin of the double resonance. Moreover, the calculation shows that the 215 cm^{-1} peak does not appear for three-dimensional molybdenum nitrides. Interestingly, the calculated phonon dispersion shows that the flat phonon dispersion appears around the K and M points in the first Brillouin zone, suggesting the possible origin of the 215 cm^{-1} peak – defect-oriented double resonance peak. The thickness dependent Raman measurements show the 215 cm^{-1} and 540 cm^{-1} peaks which are assigned to, relatively, out-of-plane and in-plane modes, gradually blue-shifts with the increase of the thickness up to 70 nm, which could be useful for characterizing the thickness of ultrathin Mo_5N_6. We also discover the thickness dependence of the 215 cm^{-1} and 540 cm^{-1} is relevant to stacking effect between the constituent layers.

INTRODUCTION

Two-dimensional (2D) materials have provided unique platforms for unconventional physics and innovative applications, due to their distinct properties compared to their three-dimensional (3D) counterparts.[1–4] Most of the studied 2D materials up to now are van der Waals (vdW) layered materials such as graphene (graphite) and transition metal dichalcogenides (TMDs).[5–8] Recently, non vdW materials have been synthesized by several methods.[9–11] Among them, the atomic-substitution-method by chemical reactions in an existing 2D material is promising for synthesizing a variety of 2D non vdW crystals, including metal nitrides[12,13],[11] metal phosphide,[13] and metal sulfides.[9] However, the properties of these 2D non vdW materials are still under explored.

Taking Mo_5N_6 as an example, the synthesis of 3D Mo_5N_6 was proposed in 1997 by using the MoS_2 powder .[14] By changing synthesis temperatures, two structures of molybdenum nitrides are formed, which were called H-MoN ($Mo_{0.96}N$) and L-MoN ($Mo_{0.82}N$).[14] The two phases are later named, respectively, as the δ-MoN and Mo_5N_6 by X-ray analysis, in which the stacking order of layers in Mo_5N_6 is assigned as the AABB structure.[15,16] In the AABB Mo_5N_6, the atoms in the direction perpendicular to the layer alternate from the prism to octahedral. Marchand *et al.*[15] further assign the space group of Mo_5N_6 as $P6_3/mmc$. While the characterization of the 3D Mo_5N_6 is investigated substantially, [15,17] the properties of 2D Mo_5N_6 have not been studied until recently when the 2D Mo_5N_6 crystals are realized[11] . In 2020, Cao *et al.*[11] performed nitridation on MoS_2 layers with a thickness of several nanometers, and synthesized thin Mo_5N_6 layers with thicknesses down to a few nanometers. Gao *et al.*,[18] further reported that the 2D Mo_5N_6 exhibits high electrical conductivity (229.6 S/cm), which could serve as a good candidate as an electrode material for 2D electronic devices.[19] Thus, it is crucial to characterize the solid-state properties of the thin Mo_5N_6 , paving the way for future applicable explorations.

So far, transmission electron microscope (TEM) and atomic force microscope (AFM) have been used to characterize, respectively, the crystal structure and thickness of the 2D Mo_5N_6.[11,18,19] However, TEM is a destructive method that requires complex sample preparation, and AFM does not generally provide information about the stoichiometry of the material. On the other hand, resonant Raman spectroscopy is a non-destructive and standard tool for nanomaterials, such as graphene, carbon nanotube, and TMDs, [20–22] which gives not-only structural properties but also solid-state properties. For example, Raman spectroscopy can analyze the number of layers,[23–25] the crystal orientation,[26,27] strain,[28,29] doping levels[30,31] and defects.[32,33] Moreover, Raman spectra, which are sensitive to the polarization direction of the incident light and temperature, provide an useful tool to probe the solid state properties of materials. These include the electronic and thermal properties.[34,35] Nevertheless, despite the reported Raman spectra of Mo_5N_6,[11,18] a more comprehensive understanding of the Raman features is needed.

In this work, the Raman spectra of Mo_5N_6 , we observed some nontrivial Raman charactetristics, especially the appearance of the Raman mode at 215 cm-1 which can not be assigned through the first order resonant Raman specroscopy calculation. In addition to the assignment of the experimentally observed Raman modes through both first-principles calculations and the Raman tensor analysis, we further discuss the origin of the 215 cm^{-1}

peak and attribute it to defect-oriented double-resonance Raman peak for the flat phonon dispersion around K to M direction in the Brillouin zone. The thickness-dependent Raman measurements show that the Raman peaks at 215 cm^{-1} and 540 cm^{-1} exhibit exponential dependency on the thickness for samples thinner than 30 nm. The large Raman frequency change of the 215 cm-1 mode with the thickness suggests a new way for thickness determination for Mo_5N_6 sample thinner than 10 nm.

Synthesis of Materials and Methods

Synthesis of 2D Mo_5N_6

The atomic substitution reaction is adopted to prepare the Mo_5N_6 by following our previous work.[11,18,19] Briefly, MoS_2 flakes with several thicknesses up to 50 nm are mechanically exfoliated from a bulk crystal using Scotch tape. Then, the flakes are transferred to a sapphire (Al_2O_3) substrate. After the sample on sapphire is transferred into a one-inch diameter quartz tube, the sample is placed in the tube furnace (Lindberg/Blue M^{TM} Mini-Mite^{TM} Tube Furnaces). Ammonium hydroxide aqua solution (30 wt%) from Fisher Scientific is loaded into the flask to generate NH_3 gas as the nitrogen source of the nitridation reaction (**Figure S1**). An Ar flow of 50 sccm is used as a carrier gas to bring NH_3 to the heating zone. The furnace is set to ramp up at the rate of 30 °C/min with the target temperature at 750 °C. The atomic substitution reaction is set to last 30 minutes to convert MoS_2 to Mo_5N_6. Mo_5N_6 with several thicknesses was obtained by controlling the thickness of precursor MoS_2 flakes, where the thicknesses are measured using AFM (Bruker DI 3000).

Raman spectroscopy measurements

The Raman spectra with laser excitiaon of 785 nm (1.58 eV) are perfemd on SENTERRA. The scattered light is collected using a SENTERRA spectrometer and a 1024-pixel-wide charge-coupled detector with a resolution less than 0.5 cm^{-1}. We can observe Raman spectra above the cut-off wavenumbers of notch-filter above 60 cm^{-1} for the 1.58eV laser excitation. The laser powers is set to be 10 mW for 1.58 eV laser excitation. [36] For the 532 nm (2.33 eV) laser excitation, we use Renishaw inVia Raman microscope and a T64 000 HORIBA micro-Raman system at room temperature with the triple monochrometer, in which we are able to measure low-frequency Raman down to 20 cm^{-1}. The duration of these Raman measurements is 300 sec with 2 accumulations.

For the 266 nm (4.66 eV) laser excitation, we collected the spectra of Mo_5N_6 using a custom-built micro-Raman setup with the laser beam focused on the sample through a 40X ultraviolet objective lens (Thorlabs, LMU-40X-UVB). The laser spot size for 266 nm laser is 1 μm. The Raman signal was collected using the same objective lens, focused into a 230 μm core fiber, and then sent to the spectrometer (Jobin-Yvan, FNR640) with a TE-cooled CCD (Andor, Newton).[36] The integration time of the measurement was 60 sec and the laser power was set to be 3.13 mW and the cut-off wavenumber is 300 cm^{-1}.

For the analysis of the phonon symmetry, we measure angular depenedent polarized Raman spectra using 532 nm laser excitation. The polar plot of Raman intensity as a function of rotating angle of linear polarizer is fitted by complex-value Raman tensor. The detail of the polarized Raman spectroscopy is given in SI (**Figure S2-S7**) .

First-principles calculations

The electronic structures and phonon dispersions of the 3D Mo_4N_4 and 2D Mo_5N_6 are calculated using the density functional theory (DFT) with the Quantum ESPRESSO package.[37] The unit-cell of 3D Mo_4N_4 consists of 4 Mo layers and 4 N layers. In the real materials, Mo vacancies are randomly distributed in the lattice with a probability of 1/6 at each Mo site, resulting in the 5:6 stoichiometry ratio of Mo and N in 2D Mo_5N_6. However, it is not possible to consider the randomly distributed defects in the DFT calculations. Thus, a defect-free Mo_4N_4 unit-cell is used for the 3D case for the DFT calculations, while for the 2D case, we adopt a supercell Mo_5N_6 containing 5 Mo layers and 6 N layers as shown in the side view of

Figure 2a.

The atomic structures of the 3D Mo_4N_4 and 2D Mo_5N_6 are shown in **Figure S8** and **Figure 2a** respectively, in which all atomic positions and lattice vectors are optimized by using the BFGS method.[38] For the 2D Mo_5N_6, a vacuum space of about 20.0 Å is set in the z-direction of the supercell to avoid the interaction between the supercell due to periodic boundary conditions. The projector-augmented-wave pseudopotentials with the Perdew-Zunger local density approximation are adopted to describe the interaction between electrons and ions.[39] The kinetic energy cutoff values for the wavefunction and charge density are 60 Ry and 800 Ry, respectively. The electron k-points (and phonon q-points) meshes taken for the 3D Mo_4N_4 and 2D Mo_5N_6 are $9 \times 9 \times 3$ and $6 \times 6 \times 2$ (and $9 \times 9 \times 1$ and $6 \times 6 \times 1$), respectively, which are selected based on the phonon frequency convergence. We adopt the truncation of the Coulomb interaction in the z-direction of the supercell for the 2D Mo_5N_6 to avoid the flexural frequency problem of the 2D system.[40]

For the 3D Mo_4N_4, four stacking geometries are possible and we label them as AAAA, AABB, AABA, and ABAB. Here, we define the AA label if the triangle of the first Mo-N layer is in the same direction as the second Mo-N layer, while the AB is defined by two triangles that are relatively rotated by 60 degrees. Since the 3D AABB Mo_4N_4 is the most stable among the four geometries, we calculate the electron and phonon dispersion for 2D Mo_5N_6 with only AABB structure.

In order to calculate the first-order resonance Raman spectroscopy of the 2D Mo_5N_6, we calculate the electron-photon M_{opt} and electron-phonon M_{ep} matrix elements using the QERaman code.[41] Then, the Raman intensity $I(E_L, E_{RS})$ is calculated as a function of the laser energy E_L and the Raman shift $E_{RS} = \hbar\omega_\nu$ as follows:

$$I(E_L, E_{RS}) = \sum_{\nu} \left| \sum_{\mathbf{k}} \sum_{i,m,m'} \frac{M_{\text{opt}}^{m'\to i}(\mathbf{k})\, M_{\text{ep}}^{m\to m'}(\mathbf{k}, \nu)\, M_{\text{opt}}^{i\to m}(\mathbf{k})}{[E_L - \Delta E_{mi}(\mathbf{k})][E_L - \Delta E_{m'i}(\mathbf{k}) - \hbar\omega_\nu]} \right|^2 \delta(E_{RS} - \hbar\omega_\nu), \quad (1)$$

where $\Delta E_{m(m')i}(\mathbf{k}) = E_{m(m')}(\mathbf{k}) - E_i(\mathbf{k}) - i\gamma$ is the energy difference between m(m′) and i states at the wavevector **k** of an electron with a resonance window γ, which is related to the lifetime of the photoexcited carrier. Here, we adopt the Lorentzian function for approximating the delta function, δ, with a finite spectral width in Eq. (1).

Results and Discussion

Experimental Raman spectra of 2D Mo_5N_6

In **Figures 1a** and **1b**, we show optical and AFM images of a typical Mo_5N_6 flake, respectively. **Figure 1c** is the AFM height profile of the flake along the white dash line shown in **Figure 1b** (AFM image). In **Figure 1d**, we show the Raman spectra of 2D Mo_5N_6 thin films from 175 cm^{-1} to 800 cm^{-1} with four thicknesses, including 2.5 nm, 4.5 nm, 15.5 nm, and 39.0 nm. A list of observed peaks are summarized in **Table S1** in SI. The Raman peak at 215 cm^{-1} shows a thickness dependence from 211 cm^{-1} to 228 cm^{-1} with changing the thickness from 2.5 nm to 39 nm, while Raman peaks at 262 cm^{-1} and 287 cm^{-1} does not show any thickness dependence as shown by dashed lines. A similar blueshift can be seen for the Raman peak at 540 cm^{-1} from 537 cm^{-1} (2.5 nm thick sample) and 545 cm^{-1} (39.0 nm thick sample). In **Figure 1e and 1f** , Raman shift of 215 cm^{-1} and 540 cm^{-1} peaks are plotted as a function of thickness, in which we can see a large increase of phonon frequency below 10 nm. Solid lines in these figures are fitted with an exponential function.

Calculated Raman spectra by first-principles calculation

First, we calculate binding energy $E_b(S)$ for the four possible stacking configurations S = AAAA, AAAB, AABB, and ABAB, as shown in **Figure S8** to obtain the stable stacking geometry, where $E_b(S)$ is defined by

$$E_b(S) = E_{\text{total}}(S) - 4E(\text{Mo}) - 4E(\text{N}), \tag{2}$$

where $E_{total}(S)$ are calculated total energies of 3D Mo_4N_4 per unit cell for the four stacking structures as shown in **Figure S8**, and E(Mo) and E(N) are, respectively, the total energies of a Mo atom in the body-centered-cubic crystal and an N atom in the N_2 molecule. The calculated results show that $E_b(S) = -5.401, -5.918, -6.024$, and -6.051 eV for S = AAAA, AAAB, AABB, and ABAB stackings, respectively, suggesting that ABAB and AABB stackings are more stable structures than AAAA and AAAB stackings. The calculated results are consistent with the previous experimental works, in which both the ABAB (or δ-MoN) and AABB stacking orders are observed in the experiment.[14] The ABAB stacking is found at a higher temperature (685°C − 1000°C),[18] while the AABB stacking is found at the comparatively lower temperature (650°C − 685°C). Although the ABAB stacking shows the largest $|E_b(S)|$, the phonon calculation at $T = 0$ K shows negative (or imaginary) phonon frequency at the M point (i.e., -150 cm^{-1}), as shown in Figure S6, suggesting it is a dynamically unstable structure. The phonon softening phenomena may be related to the observed phase transition at the temperature of 685 K .[18,42] Since the AABB structure shows a dynamically stable structure at 0 K, we can calculate phonon dispersions for both 2D (red solid line) and 3D (blue dashed line) structures as shown in **Figure 2c**. Since the optimized position of N atoms in the AABB stacking corresponds to the S atom positions in 2H-MoS_2, which serves as the solid precursor for the synthesis of Mo_5N_6 in the atomic substitution method, it is reasonable that the experimental 2D Mo_5N_6 sample has the AABB stacking order.

In **Figure 2a**, top and side views of the 2D unit cell for the AABB Mo_5N_6 are illustrated. The Mo atoms form a hexagonal structure in the ab plane, and N atoms occupy the interstitial sites of the hexagonal-close-packed Mo atoms. The 2D AABB Mo_5N_6 consists of 5 Mo and 6 N atoms in the unit cell ($a = b = 2.84$ Å), as shown in the side view of the 2D unit cell in **Figure 2d**, while the 3D AABB Mo_4N_4 crystal unit cell consists of 4 Mo and 4 N atoms, as shown in 3D unit cell ($a = b = 2.83$ Å, $c = 11.30$ Å) in Figure S6d. The 3D Mo_4N_4 crystal belongs to the D_{6h} point group[17,43] and the 2D Mo_5N_6 crystal belongs to the D_{3h} point group.

Using group theoretical analysis for the 2D AABB Mo_5N_6, we get 22 distinct phonon modes at the Γ point. The symmetry of the phonon modes is expressed by irreducible representations of D_{3h} point group as follows,

$$\Gamma_{2D} = 5A_1' + 6A_2'' + 6E' + 5E''. \tag{3}$$

A_1', E', and E'' are Raman active modes, and A_2'' is IR active mode.

In **Figure 2b**, we plot observed Raman spectra of the 2D Mo_5N_6 with a thickness of 4.5 nm by 532nm laser, in which seven phonon modes are assigned as the Raman active modes of D_{3h} by comparing with the calculated results. The phonon symmetry is confirmed by the polarized Raman measurement and the polar plot of the Raman intensity data is compared with complex-value Raman tensor analysis. The detail of polarized Raman spectra is given in SI. It is noted that the weak A_2'' mode appears at 320 cm^{-1}. Since the 2D AABB Mo_5N_6 is put on the sapphire substrate, the symmetry of the observed sample may become lower, which could be a reason why the IR active A_2'' mode can be seen.

When we compare the observed Raman spectra with the calculated phonon frequencies at the Γ point, 16 peaks are observed and listed in **Table S1**. Overall, 14 out of 16 peaks were assigned as the Γ point phonon. Note the 263 cm^{-1} is experimentally assigned to A_1' through Angular-dependent Raman analysis. The agreement between the calculated and the observed Raman peaks is satisfactory except for the most intense peak at 215 cm^{-1} in the experiment. It is clear from **Figure2c** we do not have a phonon mode for 2D Mo_5N_6 around 215cm^{-1}. A possible reason for the origin of the 215cm^{-1} peak will be discussed later.

In **Figure 2d**, we illustrate the vibration of phonon modes at 279 cm^{-1}, 533 cm^{-1}, and 698 cm^{-1}, which are assigned to the out-of-plane A_1', in-plane E'', and out-of-plane A_1' modes at the Γ point, respectively. Other 2D Mo_5N_6 phonon modes, expanding from 100 cm^{-1} to 700 cm^{-1}, are shown in **Figure S9**.

Since the observed Raman spectra show asymmetric line shape, we introduce the Breit-

Wigner-Fano (BWF) line shape to fit each line shape, as shown in **Figure S10**, which is expressed by[44]

$$I_{\mathrm{BWF}}(\omega) = I_0 \frac{(1 + \varepsilon(\omega)/q)^2}{1 + \varepsilon^2(\omega)}, \tag{4}$$

where $\varepsilon(\omega) = (\omega - \omega_0)/\gamma_0$, where ω_0 is the resonant energy, γ_0 is the effective linewidth, I_0 is the intensity at $\epsilon(\omega) = 0$, and $1/q$ is the asymmetric factor of the BWF formula. If $1/q = 0$, Eq. (4) becomes a symmetric Lorentzian shape. Thus, the fitting to the BWF line shape contains the Lorentzian line shape.

The origin of asymmetric shape is the interference effect between the phonon spectra and the continuous spectra. The asymmetric parameter ($1/q$) determines the degree and direction of asymmetry in the line shape. [45] In the fitting results, we obtain a negative $1/q$ value (shown in **Figure S10**). This means that the Raman signal on the lower-frequency side is more intense than the high-frequency side. We expect that the tail of continuous spectra of surface plasmon absorption in the lower frequency region since the 2D Mo_5N_6 is a metal. The calculated electron density of states (eDOS) in **Figure S11** also shows the metal characteristics with a finite eDOS at the Fermi energy.

Excitation energy dependence of the Raman spectra

In the experimental Raman spectra for several laser exctitations, although the peak positions of first-order Raman peaks do not change, the relative intensities change because the electron-phonon matrix element for each phonon depends on the resonant electronic wavevector k. Since we can calculate resonant Raman intensity by first-principles calculation, [41] we compare the calculated relative intensity with the observed one.

In **Figures 3**, we compare the experimental (black, top) and calculated first-order Raman spectra (color) of AABB stacking Mo_5N_6 with 266 nm (4.66 eV - deep UV), 532 nm (2.33 eV - visible light), and 785 nm (1.58 eV - near IR) laser excitations, respectively. In the calculated resonant Raman spectra, we adopt the several values of broadening factor γ in

Eq. (1) of the spectra to reproduce the relative intensity of first-order Raman spectra. The peak intensity of the calculated Raman spectra decreases with increasing γ. By comparing with the experimental Raman spectra, the $\gamma = 0.06$ eV for 1.58 and 2.33 eV laser excitations and 0.08 eV for 4.66 eV laser excitation reproduce the experimental Raman spectra with corresponding laser excitations the best. Since the lifetime of photo-excited electrons decreases with increasing the laser excitation energy, the spectrum with excitation of 4.66 eV is expected to have larger γ, which is consistent with the results mentioned above. Other calculated Raman spectra for 1.58 eV, 2.33 eV, and 4.66 eV via broadening factor, γ, are shown in **Figure S10**.

It is noted that thickness-dependent 540 cm^{-1} peak appears in the calculation and is assigned as E'' mode of Mo_5N_6. The observed peak position changes from 546 cm^{-1} with 1.58 eV laser excitation to 536 cm^{-1} with 4.66 eV laser excitation, while the calculated results of 2D M_5N_6 do not show any change of peak position as a function of laser energy. A possible reason for the peak position change of the E'' mode might come from the thickness dependence of the peak frequency in which the resonant condition for 4.66 eV (1.58 eV) appears strong for thick (thin) samples.

Since the 215 cm^{-1} peak observed under 785 nm (1.58 eV) and 532 nm (2.33 eV) excitation is not assigned to the first-order resonant Raman peak, we first consider whether the 215 cm^{-1} peak originates from double-resonance Raman (DDR) scattering. [46,47] In the DDR Raman process, non-zero phonon-wavevectors, q and $-q$ of two phonons (or one-phonon and one-elastic scattering by a defect) are relevant to the Raman spectra. In this case, when the laser excitation energy changes, the resonant q changes along the phonon dispersion.[48] Thus, by measuring the shift of peak position with changing laser energy, we could determine whether the unknown peak is a DDR peak or not. Although first-principles calculation for DDR spectra is now available,[49] the computational time of DDR spectra for a large unit cell such as Mo_5N_6 is too large. Thus we will discuss the origin of DDR spectra from phonon density of states.

Discussion of the origin of the 215 cm^{-1} Raman signal

From **Figures 1b** and 2, we have shown laser-energy-dependent Raman spectra. Here, we summarize the points for understanding the strongest Raman signal at 215 cm^{-1}.

First, as shown in **Figure 2c**, the phonon dispersion in the range of 200 to 300 cm^{-1} at the Γ point strongly depends on whether the material is 2D or 3D structure. Our Raman spectra calculation for comparison is done on the 2D structure, but the experimental Raman spectra are taken for both thin (2D) and thick (3D) samples. In fact, we will discuss later that this peak exhibits strong thickness dependence, changing from 210 cm^{-1} for 2.2 nm thick sample to 228 cm^{-1} for a > 70 nm sample on a sapphire substrate.

For the D_{3h} 2D structure, the calculated phonon frequency at 201 cm^{-1} is not Raman active A_2'' symmetry. Furthermore, for the D_{6h} 3D structure, there is a Raman inactive mode at 228 cm^{-1} with B_{2u} symmetry whose frequency is close to the 215cm^{-1} peak. We also notice that both A_1'' and A_2'' modes correspond to out-of-plane optical modes (see **Figure 4b**) in which the local volume around the Mo atom in the unit cell changes depending on the thickness. Thus, we expect that the electron-phonon matrix elements can be non-zero for the 2D structure. When we consider the five layers of 2D Mo_5N_6 in the calculation, since the volume of the unit cell does not change for the A_2'' mode, we do not get the Raman intensity.

Second, if the symmetry of the material becomes lower for some possible reasons described below, we expect the non-Raman-active mode to become Raman-active with non-zero intensity. (1) the effect of the substrate, which modifies the out-of-plane optical modes; (2) the effect of defects such as missing N or Mo atoms, interstitial atoms, which defect-oriented double resonance Raman occurs; (3) isotope of Mo atoms. Here, it is noted that the Mo atom has seven stable isotopes from ^{92}Mo to ^{100}Mo whose natural abundance are ^{92}Mo (14.84%), ^{94}Mo (9.25%), ^{95} (15.92%), ^{96}Mo (16.68%), ^{97}Mo (9.55%), ^{98}Mo (24.13%), and ^{100}Mo (9.63%).[50] The above reasons could be responsible for the appearance of the 215 cm^{-1} peak, as well as the fact that the band width of the 215 cm^{-1} is much broader than the signals from the sapphire substrate, as shown in **Figure 2b**.

Third, the flat phonon dispersion around the K point in the Brillouin zone could be another possible reason. As shown in **Figure 2c**, there are many flat phonon dispersion in the range of 200 to 300 cm^{-1} between the K and M points. It is possible that the 215 cm^{-1} mode originates from the double resonance of non-zero q phonon modes combined with a defect-induced elastic scattering. The flat phonon dispersion might be the reason why we do not see the noticeable shift of the Raman peak when changing the laser excitation from 532 nm to 785 nm. We can see from **Figure 4a**, the calculated phonon density of states has a singular value at 220 cm^{-1} for the 2D Mo_5N_6.

Luo and Xin *et al.*[51] discuss the origin of 310 cm^{-1} peak in 2H-WSe_2. 3D 2H-WSe_2 belongs to D_6h (P 6_3/mmc) and 2D 2H-WSe_2 belongs to either D_{3h} or D_{3d}, depending on the even or odd number of layers, respectively. This situation is similar to Mo_5N_6. They showed that the Raman inactive B^1_{2g}mode for 3D 2H-WSe_2 can be observed in 2D 2H-WSe_2 if the sample is defective. These results are also explained by their theoretical calculations.[51]

Moreover, other 2D materials such as SnS[52] and TiS_3[53] also show thickness-dependent Raman active B_{3g} or A_g modes. Their thickness dependence is similar to the present thickness dependence of 215 cm^{-1} and 540 cm^{-1} peaks where the phonon frequency steadily increases up to 5 layers and then becomes saturated. The phenomena is not the same for vdW and non vdW materials, since non vdW materials do not have the interlayer interaction (van-der-Waals interaction). The Raman shifting is mainly due to the change of covalent bond strength between Mo and N atoms coming from the stacking effect (i.e. compression of the lattice along the stacking direction and stretch in the other two directions).[54–56] Thus, this fully explains the blue shift of 215 cm^{-1} peak for non vdW Mo_5N_6, showing the relatively large change in phonon frequency, 18 cm^{-1}.

Conclusions

In this work, we presented a comprehensive understanding of the Raman spectra of 2D Mo_5N_6 through both experimental and theoretical approaches. The symmetry analysis of the Raman peaks is performed by the first-principles calculation of resonant Raman spectra and the angular-dependent Raman spectroscopy measurements, which is further used to assign the experimentally observed Raman peaks. In addition to the Raman peaks that are predicted by theoretical calculation, nontrivial Raman characteristics such as the appear of the 215 cm-1 mode are observed. Despite the most intensive, 215 cm^{-1} peak can not be assigned as first-order Raman peak. We attribute the 215 cm^{-1} peak to defect-oriented, double-resonance Raman peak for the flat phonon dispersion around K to M direction in the Brillouin zone. Moreover, the 215 cm^{-1} and 540 cm^{-1} peaks show a strong thickness dependence for the thickness below 10 nm. The change in frequency, 18 cm^{-1}, for the 215 cm^{-1} is relatively large compared to other 2D materials, serving as a good tool for thickness identification.

Acknowledgement

Research is primarily supported by the U.S. Department of Energy (DOE), Office of Science, Basic Energy Sciences (BES), under Award DE-SC0021064. Work by X.L. was supported by the National Science Foundation (NSF) under Grant No. (1945364) and (2111160). X.L. acknowledges the membership of the Photonics Center at Boston University. H.Z.G. acknowledges the support of BUnano Cross-Disciplinary Fellowship. R.S. acknowledges a JSPS KAKENHI Grant (No. JP22H00283) and the Yushan Fellow Program by the Ministry of Education (MOE), Taiwan. N.T.H. acknowledges financial support from the Frontier Research Institute for Interdisciplinary Sciences, Tohoku University. H.L.L. thanks the National Science and Technology Council of Taiwan for its financial support under Grants No. 112-2112-M-003-017. H.L.L. also thanks Y.M. Chang for using his deep-ultraviolet Raman

system in a portion of this work.

Supporting Information Available

Additional information for the sample preparation setup, polarized Raman spectra with comprehensive phonon symmetry analysis, calculations and simulations of the polarized Raman spectra using complex-value Raman tensors ($A_1^{'}$ mode and $E^{''}$ mode), calculated phonon dispersion for various 4 layers stacking orders of the 3D Mo_4N_4, phonon calculations expanding from 100 cm^{-1} to 700 cm^{-1} regions with the comparison to the experimental values, DOS, and calculated resonant Raman spectra as a function of the broadening factor γ.

References

(1) Bhimanapati, G. R.; Lin, Z.; Meunier, V.; Jung, Y.; Cha, J.; Das, S.; Xiao, D.; Son, Y.; Strano, M. S.; Cooper, V. R.; others Recent advances in two-dimensional materials beyond graphene. *ACS Nano* **2015**, *9*, 11509–11539.

(2) Fiori, G.; Bonaccorso, F.; Iannaccone, G.; Palacios, T.; Neumaier, D.; Seabaugh, A.; Banerjee, S. K.; Colombo, L. Electronics based on two-dimensional materials. *Nat. Nanotechnol.* **2014**, *9*, 768–779.

(3) Butler, S. Z.; Hollen, S. M.; Cao, L.; Cui, Y.; Gupta, J. A.; Gutiérrez, H. R.; Heinz, T. F.; Hong, S. S.; Huang, J.; Ismach, A. F.; others Progress, challenges, and opportunities in two-dimensional materials beyond graphene. *ACS Nano* **2013**, *7*, 2898–2926.

(4) Xia, F.; Wang, H.; Xiao, D.; Dubey, M.; Ramasubramaniam, A. Two-dimensional material nanophotonics. *Nat. Photonics* **2014**, *8*, 899–907.

(5) Manzeli, S.; Ovchinnikov, D.; Pasquier, D.; Yazyev, O. V.; Kis, A. 2D transition metal dichalcogenides. *Nat. Rev. Mater.* **2017**, *2*, 1–15.

(6) Wang, Q. H.; Kalantar-Zadeh, K.; Kis, A.; Coleman, J. N.; Strano, M. S. Electronics and optoelectronics of two-dimensional transition metal dichalcogenides. *Nat. Nanotechnol.* **2012**, *7*, 699–712.

(7) Wilson, J. A.; Yoffe, A. The transition metal dichalcogenides discussion and interpretation of the observed optical, electrical and structural properties. *Adv. Phys.* **1969**, *18*, 193–335.

(8) Balan, A. P.; Puthirath, A. B.; Roy, S.; Costin, G.; Oliveira, E. F.; Saadi, M.; Sreepal, V.; Friedrich, R.; Serles, P.; Biswas, A.; others Non-van der Waals quasi-2D materials; recent advances in synthesis, emergent properties and applications. *Mater. Today* **2022**,

(9) Du, Z.; Yang, S.; Li, S.; Lou, J.; Zhang, S.; Wang, S.; Li, B.; Gong, Y.; Song, L.; Zou, X.; others Conversion of non-van der Waals solids to 2D transition-metal chalcogenides. *Nature* **2020**, *577*, 492–496.

(10) Mounet, N.; Gibertini, M.; Schwaller, P.; Campi, D.; Merkys, A.; Marrazzo, A.; Sohier, T.; Castelli, I. E.; Cepellotti, A.; Pizzi, G.; others Two-dimensional materials from high-throughput computational exfoliation of experimentally known compounds. *Nat. Nanotechnol.* **2018**, *13*, 246–252.

(11) Cao, J.; Li, T.; Gao, H.; Lin, Y.; Wang, X.; Wang, H.; Palacios, T.; Ling, X. Realization of 2D crystalline metal nitrides via selective atomic substitution. *Sci. Adv.* **2020**, *6*, eaax8784.

(12) Anasori, B.; Lukatskaya, M. R.; Gogotsi, Y. 2D metal carbides and nitrides (MXenes) for energy storage. *Nat. Rev. Mater.* **2017**, *2*, 1–17.

(13) Wang, H.; Chen, J.; Lin, Y.; Wang, X.; Li, J.; Li, Y.; Gao, L.; Zhang, L.; Chao, D.; Xiao, X.; others Electronic modulation of non-van der Waals 2D electrocatalysts for efficient energy conversion. *Adv. Mater.* **2021**, *33*, 2008422.

(14) Tessier, F.; Marchand, R.; Laurent, Y. Preparation of transition metal nitrides using unusual routes. *J. Eur. Ceram. Soc.* **1997**, *17*, 1825–1829.

(15) Marchand, R.; Tessier, F.; DiSalvo, F. J. New routes to transition metal nitrides: and characterization of new phases. *J. Mater. Chem.* **1999**, *9*, 297–304.

(16) Maoujoud, M.; Jardinier-Offergeld, M.; Bouillon, F. Synthesis and characterization of thin-film molybdenum nitrides. *Appl. Surf. Sci.* **1993**, *64*, 81–89.

(17) Ganin, A. Y.; Kienle, L.; Vajenine, G. V. Synthesis and characterisation of hexagonal molybdenum nitrides. *J. Solid State Chem.* **2006**, *179*, 2339–2348.

(18) Gao, H.; Cao, J.; Li, T.; Luo, W.; Gray, M.; Kumar, N.; Burch, K. S.; Ling, X. Phase-controllable synthesis of ultrathin molybdenum nitride crystals via atomic substitution of MoS_2. *Chem. Mater.* **2021**, *34*, 351–357.

(19) Li, T.; Cao, J.; Gao, H.; Wang, Z.; Geiwitz, M.; Burch, K. S.; Ling, X. Epitaxial atomic substitution for MoS_2-MoN heterostructure synthesis. *ACS Appl. Mater. Interfaces* **2022**, *14*, 57144–57152.

(20) Malard, L. M.; Pimenta, M. A.; Dresselhaus, G.; Dresselhaus, M. S. Raman spectroscopy in graphene. *Phys. Reports* **2009**, *473*, 51–87.

(21) Li, H.; Zhang, Q.; Yap, C. C. R.; Tay, B. K.; Edwin, T. H. T.; Olivier, A.; Baillargeat, D. From bulk to monolayer MoS_2: evolution of Raman scattering. *Adv. Func. Mater.* **2012**, *22*, 1385–1390.

(22) Saito, R.; Tatsumi, Y.; Huang, S.; Ling, X.; Dresselhaus, M. S. Raman spectroscopy of transition metal dichalcogenides. *J. Phys. Cond. Matt.* **2016**, *28*, 353002.

(23) Berkdemir, A.; Gutiérrez, H. R.; Botello-Méndez, A. R.; Perea-López, N.; Elías, A. L.; Chia, C.-I.; Wang, B.; Crespi, V. H.; López-Urías, F.; Charlier, J.-C.; others Identification of individual and few layers of WS2 using Raman spectroscopy. *Sci. Rep.* **2013**, *3*, 1755.

(24) Malard, L.; Pimenta, M.; Dresselhaus, G.; Dresselhaus, M. Raman spectroscopy in graphene. *Phys. Rep.* **2009**, *473*, 51.

(25) Zhang, X.; Tan, Q.-H.; Wu, J.-B.; Shi, W.; Tan, P.-H. Review on the Raman spectroscopy of different types of layered materials. *Nanoscale* **2016**, *8*, 6435–6450.

(26) Ling, X.; Wang, H.; Huang, S.; Xia, F.; Dresselhaus, M. S. The renaissance of black phosphorus. *Proc. Natl. Acad. Sci. U.S.A.* **2015**, *112*, 4523–4530.

(27) Huang, M.; Yan, H.; Chen, C.; Song, D.; Heinz, T. F.; Hone, J. Phonon softening and crystallographic orientation of strained graphene studied by Raman spectroscopy. *Proc. Natl. Acad. Sci. U.S.A.* **2009**, *106*, 7304–7308.

(28) Rice, C.; Young, R.; Zan, R.; Bangert, U.; Wolverson, D.; Georgiou, T.; Jalil, R.; Novoselov, K. Raman-scattering measurements and first-principles calculations of strain-induced phonon shifts in monolayer MoS 2. *Phys. Rev. B* **2013**, *87*, 081307.

(29) Huang, M.; Yan, H.; Heinz, T. F.; Hone, J. Probing strain-induced electronic structure change in graphene by Raman spectroscopy. *Nano Lett.* **2010**, *10*, 4074–4079.

(30) Mueller, N. S.; Heeg, S.; Alvarez, M. P.; Kusch, P.; Wasserroth, S.; Clark, N.; Schedin, F.; Parthenios, J.; Papagelis, K.; Galiotis, C.; others Evaluating arbitrary strain configurations and doping in graphene with Raman spectroscopy. *2D Mater.* **2017**, *5*, 015016.

(31) Iqbal, M. W.; Shahzad, K.; Akbar, R.; Hussain, G. A review on Raman fingerprints of doping and strain effect in TMDCs. *Microelectron. Eng.* **2020**, *219*, 111152.

(32) Eckmann, A.; Felten, A.; Mishchenko, A.; Britnell, L.; Krupke, R.; Novoselov, K. S.; Casiraghi, C. Probing the nature of defects in graphene by Raman spectroscopy. *Nano Lett.* **2012**, *12*, 3925–3930.

(33) Mignuzzi, S.; Pollard, A. J.; Bonini, N.; Brennan, B.; Gilmore, I. S.; Pimenta, M. A.; Richards, D.; Roy, D. Effect of disorder on Raman scattering of single-layer MoS_2. *Phys. Rev. B* **2015**, *91*, 195411.

(34) Taube, A.; Judek, J.; Łapinska, A.; Zdrojek, M. Temperature-dependent thermal properties of supported MoS_2 monolayers. *ACS Appl. Mater. Interfaces* **2015**, *7*, 5061–5065.

(35) Judek, J.; Gertych, A. P.; Świniarski, M.; Łapińska, A.; Dużyńska, A.; Zdrojek, M. High accuracy determination of the thermal properties of supported 2D materials. *Sci. Rep.* **2015**, *5*, 12422.

(36) Gulo, D. P.; Hung, N. T.; Chen, W.-L.; Wang, S.; Liu, M.; Kauppinen, E. I.; Maruyama, S.; Chang, Y.-M.; Saito, R.; Liu, H.-L. Interacting Phonons between Layers in Raman Spectra of Carbon Nanotubes inside Boron Nitride Nanotubes. *J. Phys. Chem. Lett.* **2023**, *14*, 10263–10270.

(37) Giannozzi, P.; Baroni, S.; Bonini, N.; Calandra, M.; Car, R.; Cavazzoni, C.; Ceresoli, D.; Chiarotti, G. L.; Cococcioni, M.; Dabo, I.; others QUANTUM ESPRESSO: a modular and open-source software project for quantum simulations of materials. *J. Phys. Condens. Matter* **2009**, *21*, 395502.

(38) Hung, N. T.; Nugraha, A. R.; Saito, R. *Quantum ESPRESSO course for solid-state physics*; Jenny Stanford Publishing, New York, 2022.

(39) Perdew, J. P.; Zunger, A. Self-interaction correction to density-functional approximations for many-electron systems. *Phys. Rev. B* **1981**, *23*, 5048.

(40) Sohier, T.; Calandra, M.; Mauri, F. Density functional perturbation theory for gated two-dimensional heterostructures: Theoretical developments and application to flexural phonons in graphene. *Phys. Rev. B* **2017**, *96*, 075448.

(41) Hung, N. T.; Huang, J.; Tatsumi, Y.; Yang, T.; Saito, R. QERaman: An open-source program for calculating resonance Raman spectra based on Quantum ESPRESSO. *Comput. Phys. Commun.* **2023**, 108967.

(42) Chen, C.; Singh, B.; Lin, H.; Pereira, V. M. Reproduction of the charge density wave phase diagram in 1T-TiSe$_2$ exposes its excitonic character. *Phys. Rev. Lett.* **2018**, *121*, 226602.

(43) Sun, G.-D.; Zhang, G.-H.; Chou, K.-C. Synthesis of molybdenum nitrides nanosheets by nitriding 2H-MoS$_2$ with ammonia. *J. Am. Ceram. Soc.* **2018**, *101*, 2796–2808.

(44) Gulo, D. P.; Hung, N. T.; Yang, T.-J.; Shu, G.-J.; Saito, R.; Liu, H.-L. Exploring unusual temperature-dependent optical properties of graphite single crystal by spectroscopic ellipsometry. *Carbon* **2022**, *197*, 485–493.

(45) Hasdeo, E. H.; Nugraha, A. R. T.; Dresselhaus, M. S.; Saito, R. Breit-Wigner-Fano line shapes in Raman spectra of graphene. *Phys. Rev. B* **2014**, *90*, 245140.

(46) Pimenta, M. A.; Dresselhaus, G.; Dresselhaus, M. S.; Cançado, L. G.; Jorio, A.; Saito, R. Studying Disorder in Graphite-based Systems by Raman Spectroscopy. *Physical Chemistry Chemical Physics* **2007**, *9*, 1276–1291.

(47) Saito, R.; Grüneis, A.; Samsonidze, G. G.; Brar, V. W.; Dresselhaus, G.; Dresselhaus, M. S.; Jorio, A.; Cançado, L. G.; Fantini, C.; Pimenta, M. A.; Souza Filho, A. G. Double resonance Raman spectroscopy of single wall carbon nanotubes. *New J. Phys.* **2003**, *5*, 157.1–157.15.

(48) Saito, R.; Jorio, A.; Souza Filho, A. G.; Dresselhaus, G.; Dresselhaus, M. S.; Pimenta, M. A. Probing phonon dispersion relations of graphite by double resonance Raman scattering. *Phys. Rev. Lett.* **2002**, *88*, 027401.

(49) Huang, J.; Guo, H.; Zhou, L.; Zhang, S.; Tong, L.; Saito, R.; Yang, T.; Zhang, Z. First-principles calculations of double resonance Raman spectra for monolayer $MoTe_2$. *Phys. Rev. B* **2022**, *105*, 235401.

(50) Anbar, A. D. Molybdenum stable isotopes: observations, interpretations and directions. *Rev. Mineral. Geochem.* **2004**, *55*, 429–454.

(51) Luo, X.; Zhao, Y.; Zhang, J.; Toh, M.; Kloc, C.; Xiong, Q.; Quek, S. Y. Effects of lower symmetry and dimensionality on Raman spectra in two-dimensional WSe_2. *Phys. Rev. B* **2013**, *88*, 195313.

(52) Li, M.; Wu, Y.; Li, T.; Chen, Y.; Ding, H.; Lin, Y.; Pan, N.; Wang, X. Revealing anisotropy and thickness dependence of Raman spectra for SnS flakes. *RSC Adv.* **2017**, *7*, 48759–48765.

(53) Lipatov, A.; Loes, M. J.; Lu, H.; Dai, J.; Patoka, P.; Vorobeva, N. S.; Muratov, D. S.; Ulrich, G.; Kastner, B.; Hoehl, A.; others Quasi-1D TiS_3 nanoribbons: mechanical exfoliation and thickness-dependent Raman spectroscopy. *ACS Nano* **2018**, *12*, 12713–12720.

(54) Zhou, S.; Wang, R.; Han, J.; Wang, D.; Li, H.; Gan, L.; Zhai, T. Ultrathin non-van der Waals magnetic rhombohedral Cr_2S_3: space-confined chemical vapor deposition synthesis and Raman scattering investigation. *Adv. Func. Mater.* **2019**, *29*, 1805880.

(55) Zhao, Y.; Qiao, J.; Yu, P.; Hu, Z.; Lin, Z.; Lau, S. P.; Liu, Z.; Ji, W.; Chai, Y. Extraordinarily strong interlayer interaction in 2D layered PtS_2. *Adv. Mater.* **2016**, *28*, 2399–2407.

(56) Li, H.; Zhang, Q.; Yap, C. C. R.; Tay, B. K.; Edwin, T. H. T.; Olivier, A.; Baillargeat, D. From bulk to monolayer MoS_2: evolution of Raman scattering. *Adv. Func. Mater.* **2012**, *22*, 1385–1390.

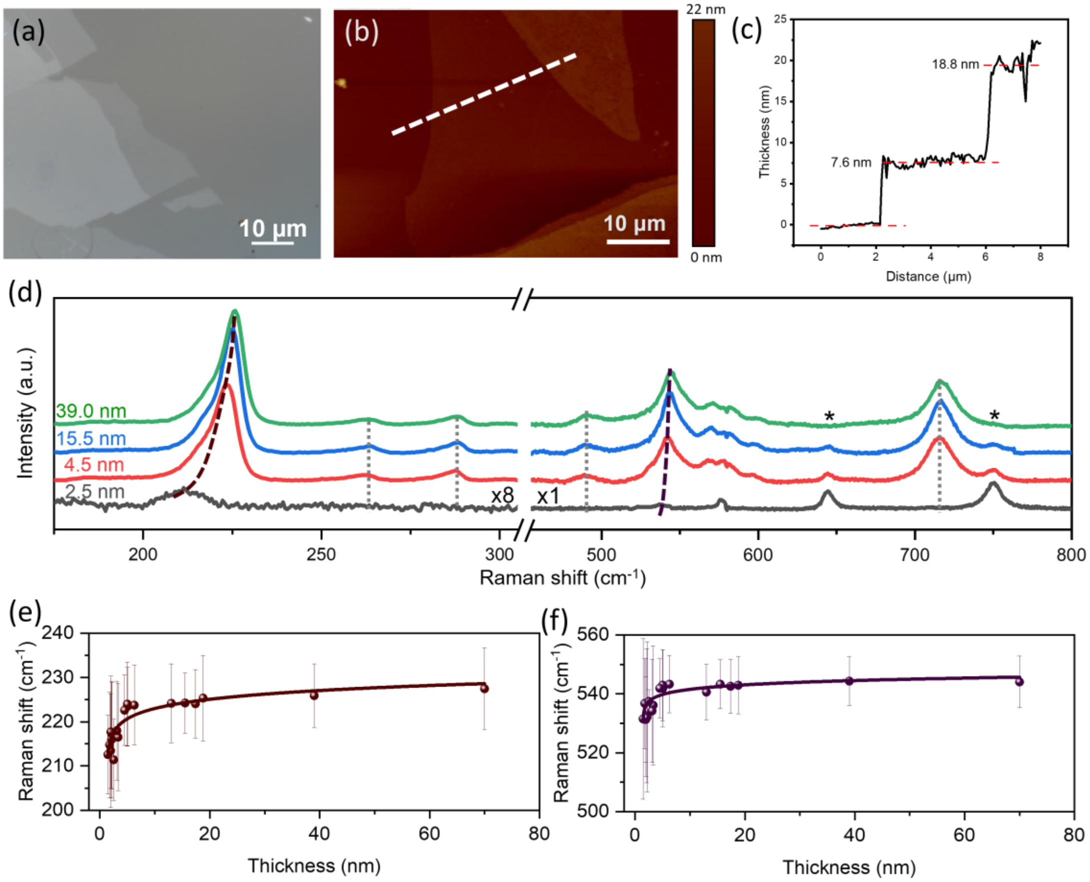

Figure 1: Investigation of the thickness-dependent Raman spectra of Mo_5N_6 under 532 nm laser excitation. (a) Optical microscope image of Mo_5N_6 on a sapphire substrate. (b) AFM image of the Mo_5N_6 sample shown in (a). (c) The height profile of the AFM image is shown on (b) white dashed line. (d)Raman spectra of Mo_5N_6 with four different thicknesses: 2.5 nm (black), 4.5 nm (red), 15.5 nm (blue), and 39.0 nm (green). The dash lines are eye guides to show the thickness-dependent shift of the modes. Peaks marked with (⋆) are from the sapphire substrate. (e)-(f) Raman shift as a function of the thickness of the correlated phonon modes shown in (d). The lines indicate the trend of the dependence.

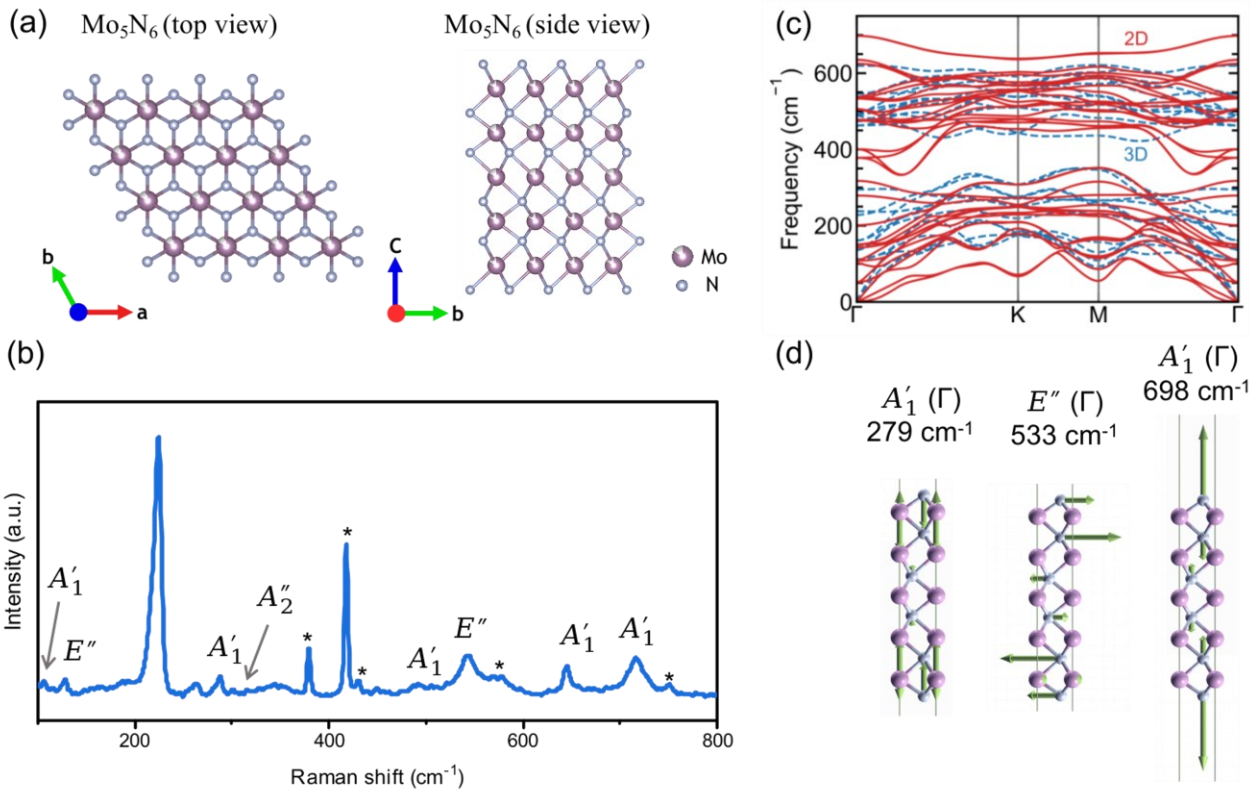

Figure 2: Crystal structure, Raman spectra, and phonon dispersion of Mo_5N_6. (a) Top view and side view of 2D Mo_5N_6 crystal structure with the AABB arrangement of nitrogen atoms (shown in the side view). (b) Experimental Raman spectra of Mo_5N_6, measured under 532 nm laser, with eight peaks assigned with their phonon symmetries. Peaks marked with (*) signal are from the sapphire substrate. The strongest Raman signal is marked as $\star$ (c) DFT calculated phonon dispersions of AABB stacked 2D (red solid line) and 3D (blue dashed line) Mo_5N_6. (d) Selected Raman modes and their corresponding symmetries and vibrations for the 2D Mo_5N_6.

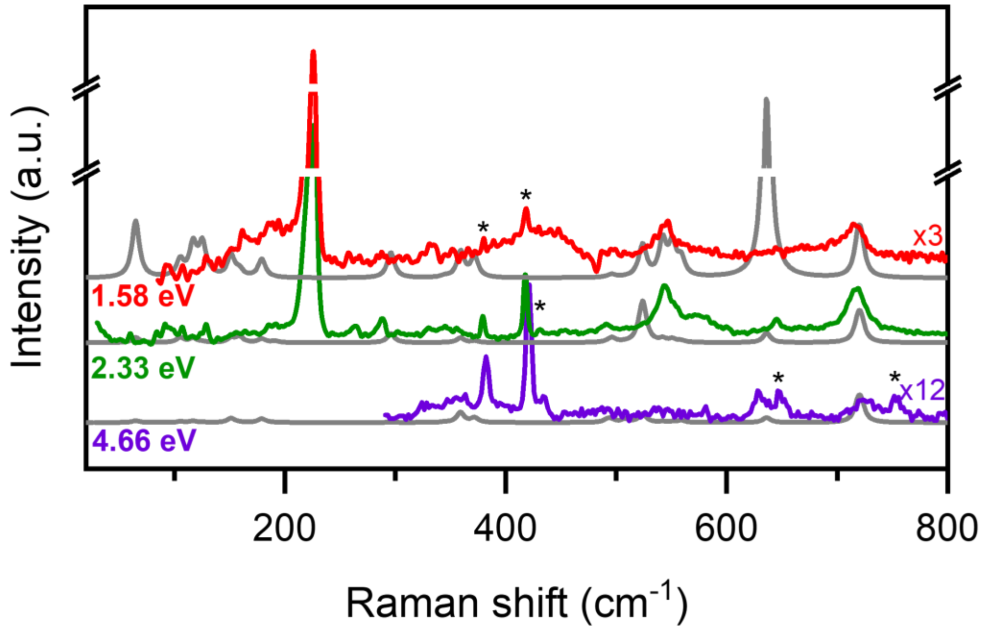

Figure 3: 2D Mo_5N_6 laser excitation dependent experimental data and the calculated Raman spectra with γ = 0.06 eV for 532 nm (2.33 eV), and 785 nm (1.58 eV) laser excitations and γ = 0.08 eV for 266 nm (4.66 eV) laser excitation. Note the colored spectra are the experimental data, and the grey ones are γ dependent calculations.

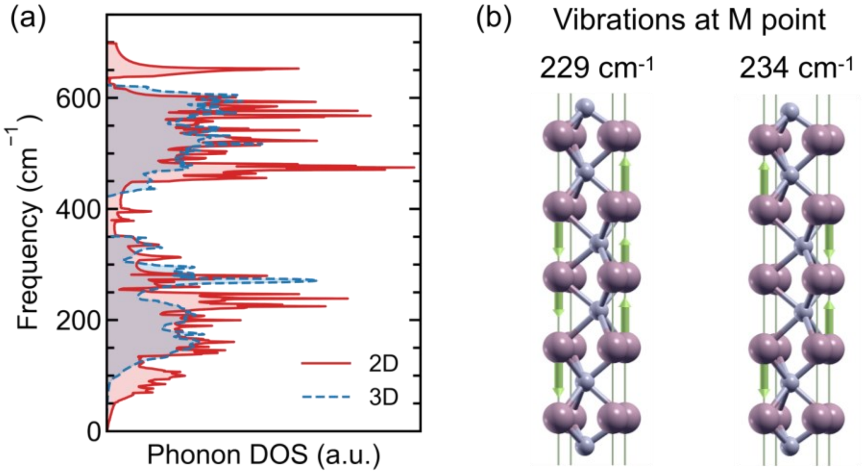

Figure 4: Calculated phonon density of states and assigned vibration modes at the M point. (a) Phonon DOS of 2D Mo_5N_6 (red solid line) and 3D Mo_5N_6 (blue dash line). (b) 229 and 234 cm^{-1} M point vibration modes of 2D Mo_5N_6.